Supplementary information for

Panther chameleon-inspired Vis-NIR light modulation hydrogel with enhanced photothermal effect and pH/temperature monitoring for bacterial infection theranostics

Zixin Shu, [a] Yang Yun, [b] Xiaoning Sun, [a] Jing Cheng, [a] Chuanshun Hu, [a] Xu Peng, [c] Xinyuan Xu, [a] Meng Su, [b] Meng Qin *[a] and Jianshu Li *[ade]

[a] College of Polymer Science and Engineering, State Key Laboratory of Advanced Polymer Materials, Sichuan University, Chengdu 610065, China

[b] Key Laboratory of Green Printing, CAS Research/Education Center for Excellence in Molecular Sciences, Institute of Chemistry, Chinese Academy of Sciences, Beijing 100190, P. R. China

[c] Experimental and Research Animal Institute, Sichuan University, Chengdu 610065, China

[d] State Key Laboratory of Oral Diseases, West China Hospital of Stomatology, Sichuan University, Chengdu 610041, China

[e] Med-X Center for Materials, Sichuan University, Chengdu 610041, China

[*] **Correspondence authors.**

E-mail: qinmeng@scu.edu.cn, jianshu_li@scu.edu.cn.

Experimental section

Materials

Styrene (St) was purchased from Tianjin Fuchen Chemical Reagents Co., Ltd. Methyl methacrylate (MMA) and potassium persulfate (KPS) were purchased from Tianjin Bodi Chemical Co., Ltd. Hydrochloric acid (HCl) was purchased from Chengdu Kelong Chemical Co., Ltd. Phosphate-buffered saline (PBS) powder was purchased from Saivier Biotechnology Co., Ltd. Acrylic acid (AA), sodium dodecyl benzene sulfonate (SDBS), acrylamide (AAm), *N, N'*-methylenebisacrylamide (BIS), 2-hydroxy-2-methylpropiophenone (HMPP), methacrylic anhydride (MA), dimethylaminoethyl methacrylate (DMAEMA), and carbon black (CB) were purchased from Shanghai Macklin Biochemical Technology Co., Ltd. Sodium bisulfite ($NaHSO_3$) and sodium hyaluronate (SH, MW ~ 90–100 kDa) were purchased from Shanghai Yuanye Bio-Technology Co., Ltd.

Preparation of monodispersed poly(styrene-methyl methacrylate-acrylic acid) nanoparticles and photonic crystal templates

Monodisperse composite latex nanoparticles of poly(styrene-methyl methacrylate-acrylic acid) were synthesized by soap free emulsion copolymerization according to the literature.[1] Typically, St, MMA, AA, SDBS, NH_4HCO_3, and ultrapure water were added sequentially to a three-necked flask with a mechanical stirrer moving at 300 rpm. Reaction of the mixture was initiated at 70 ^oC for 30 min. Following the addition of an aqueous solution of KPS (3.6 wt.%), polymerization was carried out at 80 ^oC for 4 h to obtain a homogeneous latex with monodispersed nanoparticles. The as-synthesized poly(styrene-methyl methacrylate-acrylic acid) composite latex nanoparticles were used without further purification. The diameters of 231.4 nm and 338.5 nm were adjusted by adding SDBS 20 mg and 15 mg, respectively.

Photonic crystal templates were fabricated by vertical deposition of poly(styrene-methyl methacrylate-acrylic acid) suspension.[2] Briefly, clean glass slides were

immersed vertically into a glass bottle filled with the 0.1 wt.% suspension of poly(styrene-methyl methacrylate-acrylic acid) nanoparticles. Subsequently, the glass bottle was placed in a constant temperature and humidity chamber at a constant temperature of 60 °C with a relative humidity of 60% for more than 72 h. Finally, the photonic crystal templates self-assembled from poly(styrene-methyl methacrylate-acrylic acid) nanoparticles were obtained.

Synthesis of HAMA

HAMA was fabricated through the previously described method.[3] Briefly, 1 g SH was dissolved into ultrapure water in a round bottom flask followed by dropping 2.5 mL MA into the solution. NaOH solution (5 N) was used to maintain the alkaline pH (8–9). After stirred continuously overnight at 4 °C, the obtained solution was dialyzed against ultrapure water for three days for purification. The HAMA product was lyophilized and stored at 4 °C for further studies.

Preparation of DSPCH

Typically, a clean glass was placed above D-template with 200 μm space in between. Then, UV-initiated precursor solution containing HAMA, AAm, BIS, CB, HMPP and ultrapure water was filled into the space between two glass slides due to capillary force. After UV (365 nm) irradiation for 10 s, the two glass slides were carefully separated and the D-PCH was obtained. Subsequently, the S-template was placed above the as-prepared D-PCH with 200 μm space in between. Then, S-PCH precursor solution containing DMAEMA, BIS, APS, $NaHSO_3$ and ultrapure water was filled into the space between S-template and D-PCH. After initiated in 4 °C overnight, the two slides were carefully separated and as-prepared DSPCH was peeled off from the glass slide.

Characterization

The scanning electron microscopy (SEM) images of templates and hydrogels were

acquired using an Apreo S HiVoc microscope (ThermoFisherScientific). The morphology of interface between the dual-layer hydrogels was characterized using the cryo-electron microscopy mode. The structures of SH and HAMA were characterized by a ^{1}H NMR spectrum recorded on an AV III HD 400 MHz NMR spectrometer (Bruker). The transmittance and reflectance spectra were measured using a UV-Vis spectrometer (UV-2600i) with an integrating sphere. The optical photographs were taken using a cell phone. The *R*, *G*, *B* values of the images were extracted using software ImageJ (Fiji). The CIE plots were analyzed from the measured reflectance spectra.

Enhanced photothermal properties and calculation of PCE

PCH_0, PCH_{585}, and PCH_{820} were irradiated by 808 nm laser at various light power densities (0.19, 0.23, 0.28, 0.33 W cm^{-2}) for 10 min and the corresponding thermal images were recorded using a thermal camera.

For the overall photothermal performance of DSPCH, the photothermal curves were recorded under NIR irradiation (0.33 W cm^{-2}, 5 min). Additionally, the stability of photothermal conversion was assessed by four repeated heating-cooling NIR irradiation. The stability of D-layer PBG was evaluated through immersing DSPCH into various PBS solutions under different pH/temperature conditions and measuring the corresponding reflectance spectra.

PCE (η) was calculated through the following equations reported previously[4]:

$$\eta = \frac{hS(T_{max} - T_{min})}{I} \times 100\% \#(1)$$

$$hS = \frac{mC_p}{\tau_s} \#(2)$$

$$\tau_s = -\frac{t}{ln\theta} \#(3)$$

$$\theta = \frac{T_i - T_{min}}{T_{max} - T_{min}} \#(4)$$

where h is the heat transfer coefficient; S is the surface area; T_{max}, T_{min} are the maximum heating and final cooling temperature of hydrogels, respectively; I is the laser power (0.51 W, which is transferred from light power density 0.33 W cm^{-2}); θ is a driving force temperature; m is the mass of hydrogel (0.04 g); C_p is specific heat capacity of hydrogel (≈ 4.2 J g^{-1} $^oC^{-1}$); t is the cooling time; T_i is the real-time temperature of each t; τ_s is the sample system time constant, which is calculated through cooling curves (Figure S6, Supporting Information).

Finite element analysis

The full-wave-simulation using a commercial software COMSOL was performed to investigate the photothermal power.[5,6] CB-loaded photonic hydrogel 3D matrix (30 layers of face-centered close packing photonic crystal nanospheres) was stacked along the z-axis. Periodic boundary conditions were adopted along lateral faces. The port boundary condition was set at the top of the model to simulate the vertical NIR irradiation and absorb the reflected light while another port boundary condition was set at the bottom of the model to absorb the transmission light. The electric field distribution in the PCH matrix was investigated under NIR irradiation through a formulating derivation of Helmholtz equation:

$$\nabla \times \mu_r^{-1}(\nabla \times E) - k_0^2\left(\epsilon_r - \frac{j\sigma}{\omega\epsilon_0}\right)E = 0 \#(5)$$

where ∇ is Hamiltonian; μ_r is relative permeability; E is electric field intensity; k_0 is free-space wavenumber; ϵ_r is relative permittivity; σ is conductivity; ϵ_0 is vacuum permittivity; ω is angular frequency. The photothermal power (Q) was further calculated through equation:

$$Q = \frac{1}{2}Re\left(i\omega B \cdot H^*\right) + \frac{1}{2}Re\left(\sigma|E|^2\right) \#(6)$$

where B is the magnetic flux density and H^* is the complex conjugate of magnetic field intensity.

Evaluation of pH responsiveness

Typically, DSPCHs with the same initial reflectance wavelengths were separately immersed into PBS solutions with various pH (4, 5, 6, 7, 8, 9). Different buffer solutions were prepared by using 1N HCl or 1N NaOH aqueous solutions to correct the pH of original PBS solutions (pH 7). After 30 min, DSPCHs were taken out from the solutions and wiped dry with filter paper. The reflectance spectra were measured through a fiber spectrometer (FX2000) and the optical images were recorded.

To evaluate the reversibility and real-time pH sensing capability, DSPCH was alternately immersed in acidic (pH 5), neutral (pH 7), and alkaline (pH 8) PBS solutions (sequence: 5→7→8→7→5) for three cycles. DSPCH was soaked in each solution for 5 min, with the reflectance spectra measured every minute.

To simulate the environment of wounds, artificial wound exudates were prepared according to previous reported method by dissolving sodium chloride (128.83 mmol L^{-1}), magnesium chloride (0.94 mmol L^{-1}), calcium chloride (2.23 mmol L^{-1}), sodium bicarbonate (19.00 mmol L^{-1}), glucose (1.80 mmol L^{-1}), albumin (22 g L^{-1}), potassium chloride (4.40 mmol L^{-1}), urea (8.90 mmol L^{-1}), uric acid (0.35 mmol L^{-1}), and sodium lactate (10.90 mmol L^{-1}) in ultrapure water according to previous methods.[7] 1N HCl or 1N NaOH solutions were used to adjust pH, which was calibrated by a pH meter.

Evaluation of temperature responsiveness

Similar to pH assays, the temperature responsiveness of DSPCH was conducted by immersing DSPCHs with the same initial reflectance wavelengths into PBS solutions with varying temperatures (35, 40, 45, 50, 55, 60 ^{o}C).

To evaluate the overheating warning ability, DSPCH was initially immersed in the PBS solution at 35 ^{o}C to reach the equilibrium. Subsequently, DSPCH was swiftly transferred into PBS solution at 55 ^{o}C, during which the reflectance spectra were

measured every 15 s.

To evaluate the stability and reversibility, reflectance spectra were measured with four 35-60 ^{o}C cycles.

Cytocompatibility evaluation

Mouse fibroblasts (L929) cells were used to assess the cytotoxicity of DSPCH through Cell Counting Kit-8 (CCK8) and Dual-fluorescence cell viability assay. The DSPCH extracts were obtained by immersing DSPCH in a α-MEM medium containing 10% FBS, 1% penicillinstreptomycin solution and for 24 h.

For CCK-8 assay, L929 cells (1.0×10^4 cells per well) were seeded in a 96-well plate and cultured for 24 h. Then, the cell culture medium was replaced with the extracts and cultured for 1 d, 3 d (37 ^{o}C, 5% CO_2). After removing the culture supernatants, fresh medium containing 10% CCK-8 agent was added to each well. After 2 h in the dark, the media was transferred to a new 96-well plate. The optical density at 450 nm was then measured using a microplate reader (KHB ST-360, China). Cell proliferation ratio was calculated using the following formula:

$$Cell\ proliferation\ ratio\ (\%) = \frac{\left(A_s(x) - A_b(1)\right)}{\left(A_c(1) - A_b(1)\right)} \times 100\%\#(7)$$

where A_s (x) is the absorbance of the DSPCH group at different time points (x = 1, 3), $A_c(1)$ is the absorbance of the control group (without DSPCH extracts) on day 1, and $A_b(1)$ is the absorbance of the blank control group (without sample extracts or cells) on day 1.

For live/dead staining, L929 cells were seeded in a 48-well plate and initially cultured for 24 h, and then cocultured with the extracts for 1 d, 3d. After the culture supernatants were removed, fluorescein diacetate /propidium iodide staining solution, was added and cocultured in the dark for 30 min. After a final PBS rinse, the stained live/dead cells were then imaged using an inverted fluorescence microscope (IX-71, Olympus, Japan).

In vitro hemolysis assay

The blood from rats was mixed with ultrapure water (positive control group), PBS (negative control group), and PBS extract of DSPCH at a concentration of 50 mg mL^{-1}, respectively. After the incubation at 37 °C for 1 h, these mixtures were centrifuged at 1000 rpm min^{-1} for 5 min. Finally, the optical densities of the supernatants from various groups were measured at 545 nm using a microplate reader. The hemolysis ratio was calculated using the following formula:

$$Hemolysis\ ratio\ (\%) = \frac{(OD_{sample} - OD_{negative})}{(OD_{positive} - OD_{negative})} \times 100\% \#(8)$$

In vitro antibacterial assays

Staphylococcus aureus (*S. aureus*, ATCC29213, Nanjing Kobai Biotechnology Co.) and *Escherichia coli* (*E. coli*, ATCC35218, Shanghai Fuxiang Biotechnology Co.) were employed as the typical Gram-positive and Gram-negative bacteria, respectively, to evaluate *in vitro* photothermal antibacterial efficacy of DSPCH. The groups were divided into six groups (n = 3): (1) PBS−, (2) $DSPCH_0$−, (3) $DSPCH_{820}$−, (4) PBS+, (5) $DSPCH_0$+, (6) $DSPCH_{820}$+, where "+" and "–" represent with and without NIR irradiation, respectively. Typically, ultraviolet-sterilized hydrogel discs (diameter 8 mm, thickness 400 μm) were added to each well of the plate and were immersed by 500 μL suspension of *S. aureus* (1.0×10^6 CFU mL^{-1}). *E. coli* suspension was treated in the same way. For each NIR+ group, NIR laser irradiation (light power density: 0.33 W cm^{-2}) was applied for 10 min. After various treatments, the bacterial suspension of each group was used for subsequent plate counting, live/dead bacterial fluorescence staining, and SEM observation.

Plate Counting Method: After the treatment, bacterial suspension of each group was diluted 1.0×10^3 times by sterile PBS. Then, 100 μL of each diluted bacterial solution

was spread onto solid agar plates (n = 3). The plates were incubated at 37 °C overnight, and the colony images were recorded using a cell phone. The colonies were counted by software ImageJ. Bacterial viability was calculated by counting the colony numbers on the agar plates, using the following formula:

$$Bacterial\ viability\ (\%) = {}^{N_{sample}}/_{N_{control}} \times 100\% \#(9)$$

where N_{sample} represents the colony number of each group, and N_{control} represents that of PBS− group.

Live/dead Bacterial Fluorescence Staining: After various treatment, the mixtures were stained using the live/dead Bacterial Assay Kit for 30 min in the dark, and then observed under an inverted fluorescence microscope for green fluorescence (NucGreen for live bacteria) and red fluorescence (EthD-III for dead bacteria).

SEM observation: The treated bacterial solutions were fixed with 4% glutaraldehyde overnight, followed by dehydration using a graded ethanol series (30%, 50%, 70%, 90%, 100%). Finally, the bacteria solutions were dried and sputter-coated for SEM observation.

In vivo wound healing assays

The SD rats (female, 200 g) were provided and maintained by the Laboratory Animal Center of Sichuan University. All animal experiments were carried out with the permission of Animal Research Committee of Sichuan University (approved No. KS2021515). On day −2, the full-thickness round skin wounds (×2, diameter 1 cm) were created on the back of each rat to establish an infection model. Then, 100 μL of *S. aureus* suspension (1.0×10^8 CFU mL^{-1}) was dropped to the circular wound bed for wound infection and purulence. On day 0, the rats were randomly divided into six groups (n = 3): (1) 3M−, (2) $DSPCH_0$−, (3) $DSPCH_{820}$−, (4) 3M+, (5) $DSPCH_0$+, (6) $DSPCH_{820}$+, where 3M means treated with 3M polyurethane dressings only, and hydrogel groups were treated with $DSPCH_0$, $DSPCH_{820}$, respectively, fixed with 3M

dressings. Additionally, 808 nm laser was used to treat the NIR+ groups (light power density: 0.33 W cm^{-2}) on days 0, 6, and the temperature variations were recorded using a thermal imaging camera. The structural color changes of $DSPCH_{820}$ responded to wound pH within 30 min were recorded and compared with the results of pH test paper on days −2, 0, 3 ,6. The representative images of wounds were photographed and the wound areas were analyzed using software ImageJ. The wound healing rates were calculated by the formula:

$$Wound\ healing\ rate\ (\%) = \left[(A_0 - A_t)/A_0\right] \times 100\%\#\ （10）$$

where A_0 is the initial wound area and A_t is the wound area on day n (n = 0, 3, 6, 8, 10). On day 3, bacteria from the wound were collected using the sterile swabs and plate counting assay was conducted to assess the *in vivo* photothermal antibacterial afficacy. All rats were executed on day 10. The wound bed tissues and major organs (heart, liver, spleen, lungs, and kidneys) were harvested and fixed in 4% paraformaldehyde for further histological analysis, including H&E staining, Masson staining and immunofluorescence staining for IL-6 and CD31.

Figures and tables

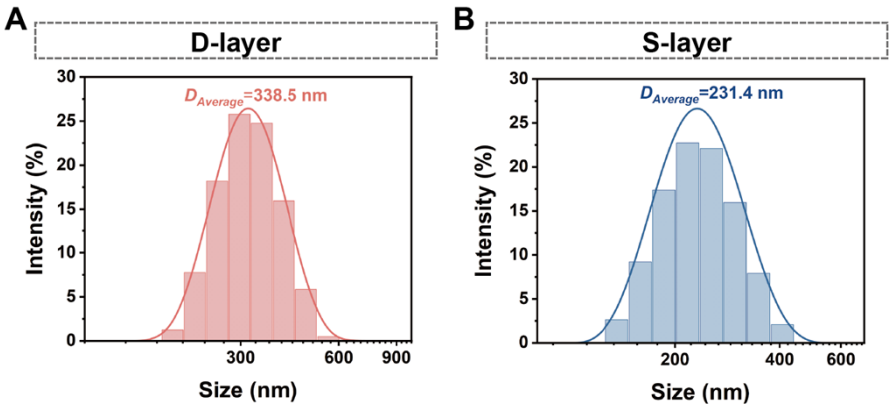

Fig. S1 Diameter distribution histograms of poly(styrene-methyl methacrylate-acrylic acid) nanoparticles for (A) D-layer and (B) S-layer of DSPCH.

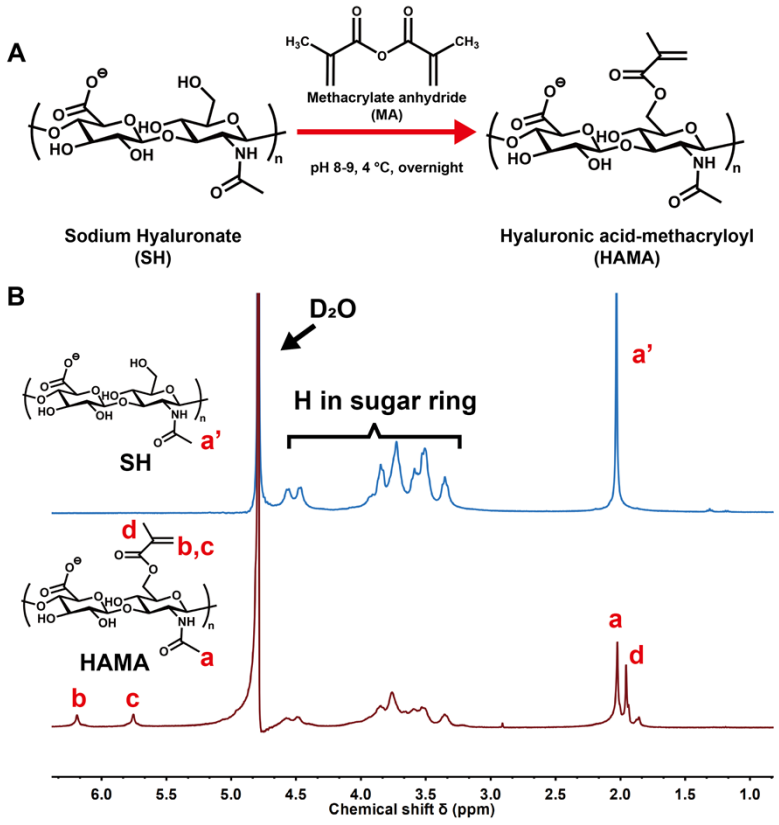

Fig. S2 (A) Schematic synthesis of HAMA. (B) ^{1}H-NMR spectra of SH and HAMA.

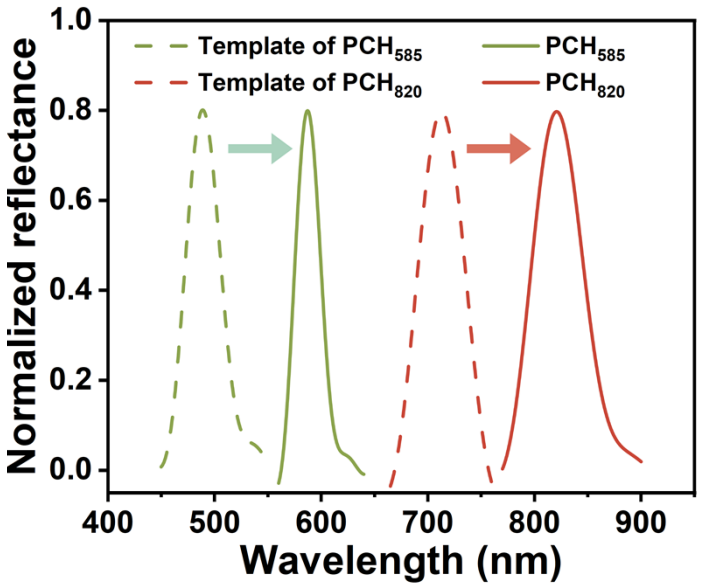

Fig. S3 Reflectance spectra of PCH_{585} and PCH_{820}, prepared through the photonic crystal templates with reflectance peaks located at 488 nm and 715 nm, respectively.

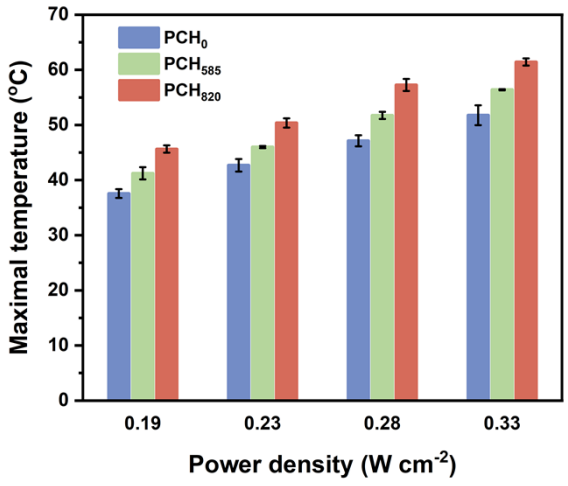

Fig. S4 Maximal temperatures of PCH_0, PCH_{585}, and PCH_{820} after 808 nm NIR irradiation at different power densities for 5 min.

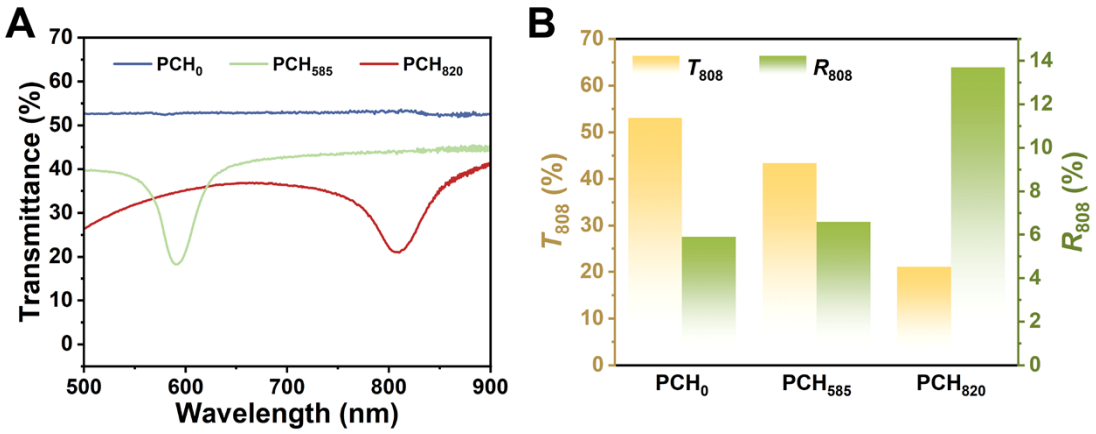

Fig. S5 (A) Transmittance spectra of PCH_0, PCH_{585}, and PCH_{820}. (B) Transmittance and reflectance at 808 nm (denoted as T_{808} and R_{808}, respectively) at 808 nm of PCH_0, PCH_{585}, PCH_{820}.

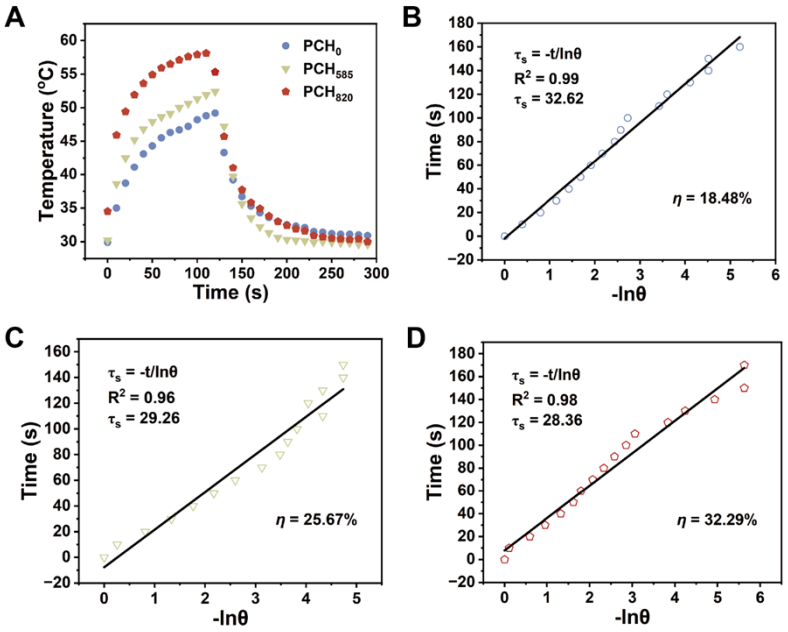

Fig. S6 (A) Heating-cooling curves of PCH_0, PCH_{585}, and PCH_{820}. (B–D) Time constants for heat transfer of (B) PCH_0, (C) PCH_{585}, and (D) PCH_{820}, calculated *via* the cooling portion from (A).

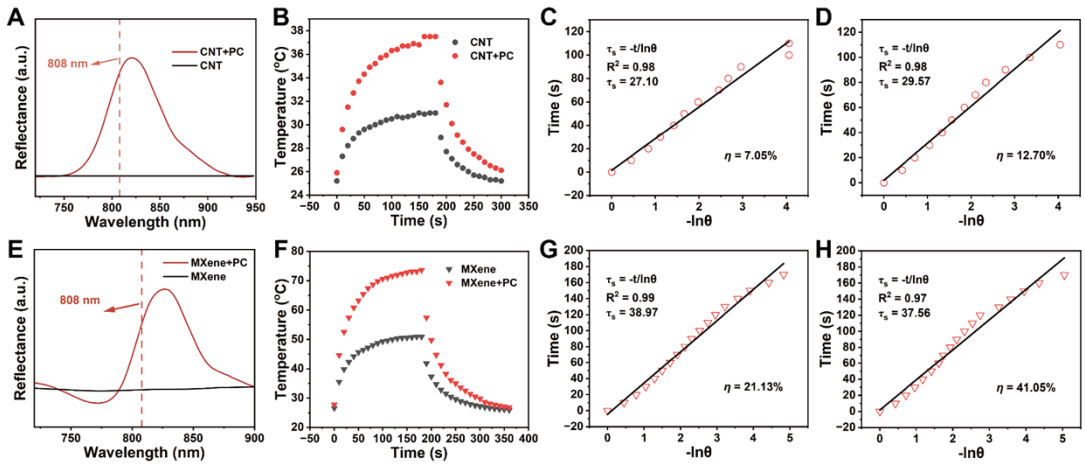

Fig. S7 (A) Reflectance spectra and (B) heating-cooling curves of CNT-based hydrogels with or without PC. Time constants for heat transfer of CNT-based hydrogels (C) without or (D) with PC. (E) Reflectance spectra and (F) heating-cooling curves of MXene-based hydrogels with or without PC. Time constants for heat transfer of MXene-based hydrogels (G) without or (H) with PC.

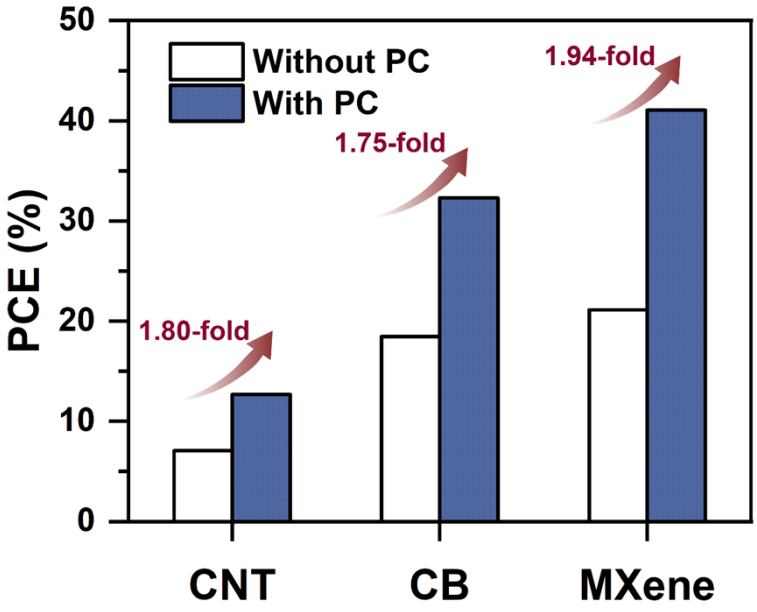

Fig. S8 PCE and PCE enhancement of CNT-, CB-, and MXene-based hydrogels with or without PC.

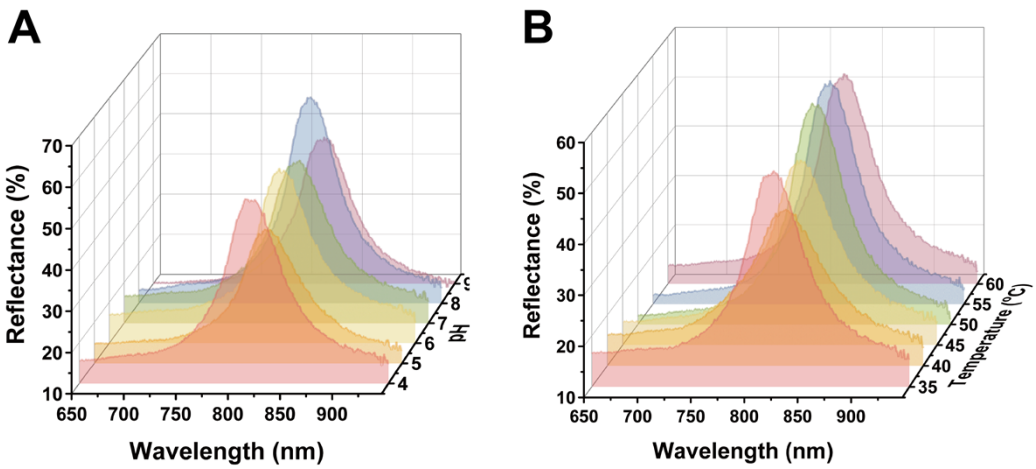

Fig. S9 Reflectance spectra of D-PCH at different (A) pH and (B) temperature conditions.

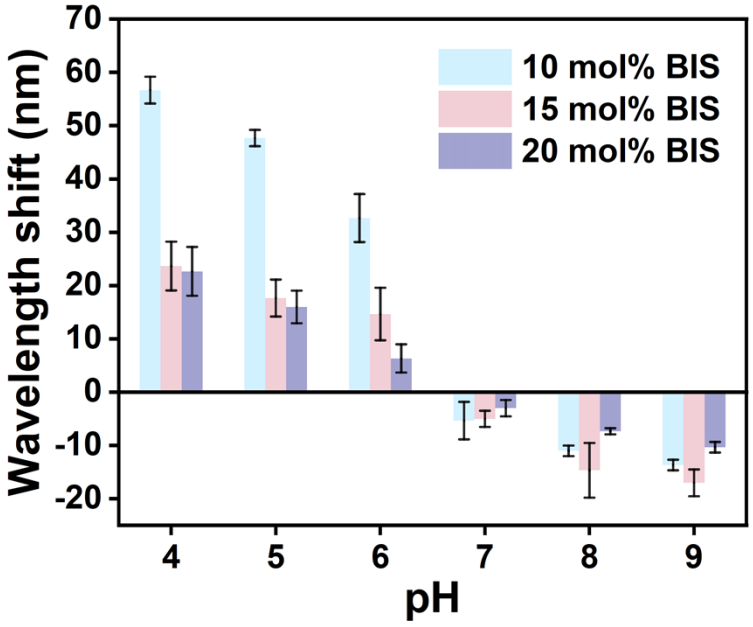

Fig. S10 Reflectance wavelength shifts (compared to the initial state) of PDMAEMA-based photonic crystal hydrogels with various concentrations of BIS at different pH.

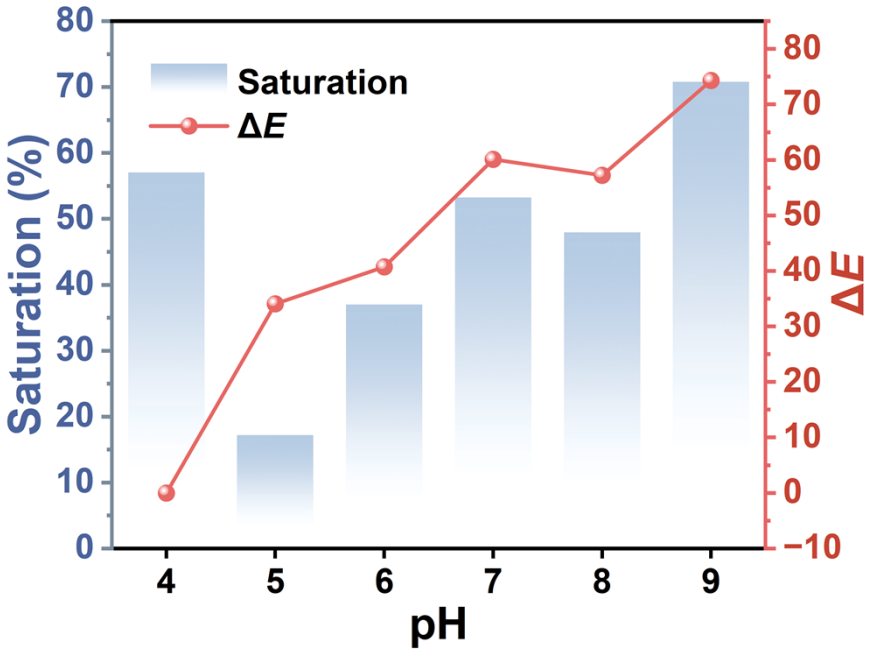

Fig. S11 Structural color saturation and Δ*E* of DSPCH at different pH conditions.

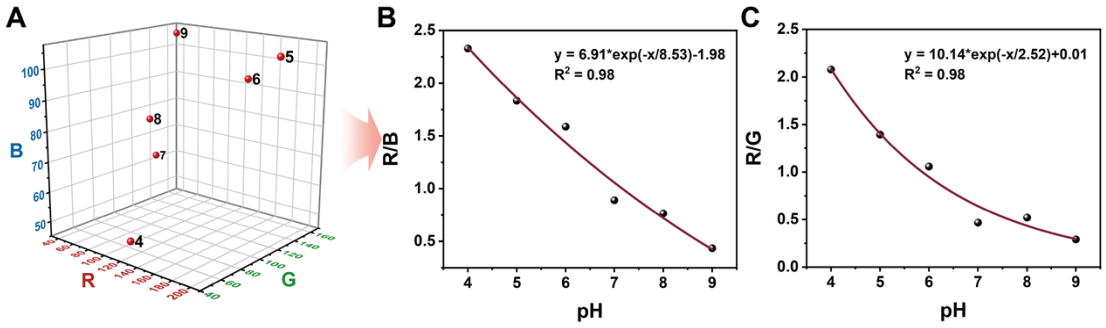

Fig. S12 (A) *RGB* space of DSPCH at different pH values. (B) The correlation fitted between *R*/*B* values of DSPCH and pH. (C) The correlation fitted between *R*/*G* values of DSPCH and pH.

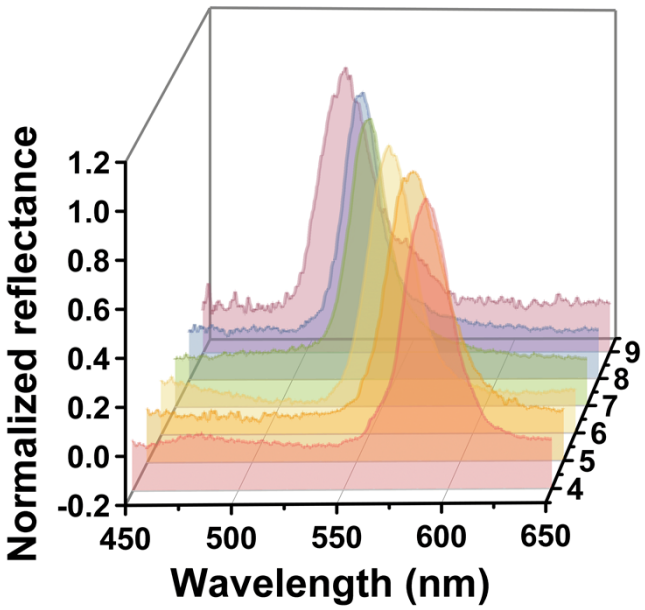

Fig. S13 Reflectance spectra of DSPCH in artificial wound exudates with different pH.

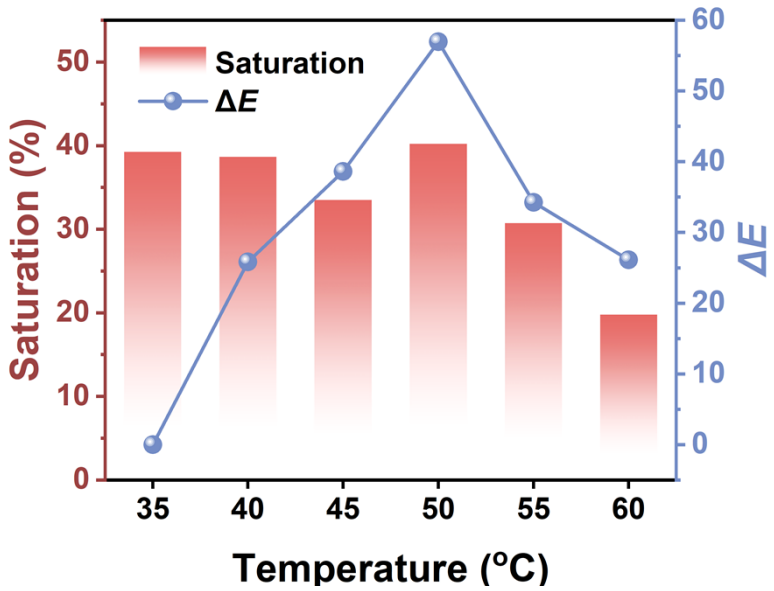

Fig. S14 Structural color saturation and Δ*E* of DSPCH at different temperatures.

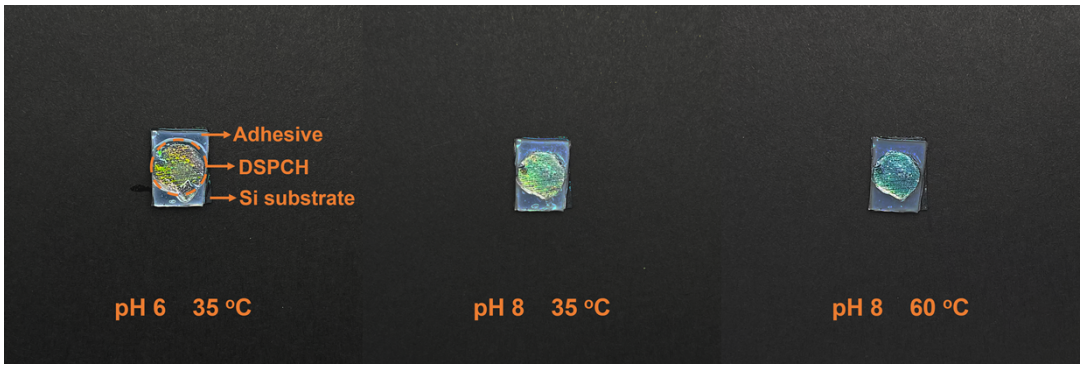

Fig. S15 Representative uncropped photographs of the circular DSPCHs fixed on the Si substrate using an adhesive at various pH and temperature conditions.

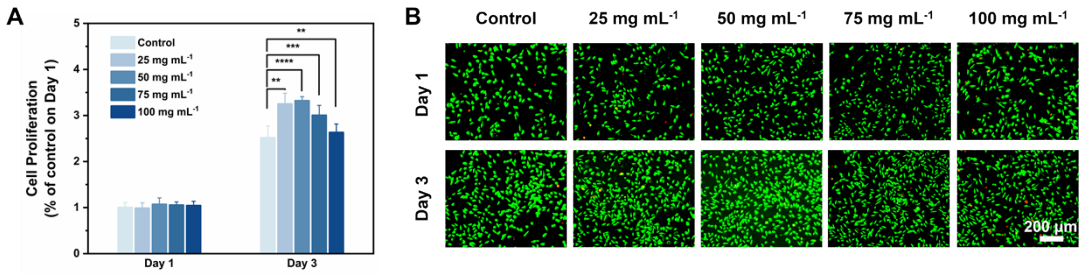

Fig. S16 (A) Cell proliferation of L929 cells after incubation with DSPCH extracts at different concentrations for 3 d. (B) Representative fluorescent images of live (green) and dead (red) staining L929 cells.

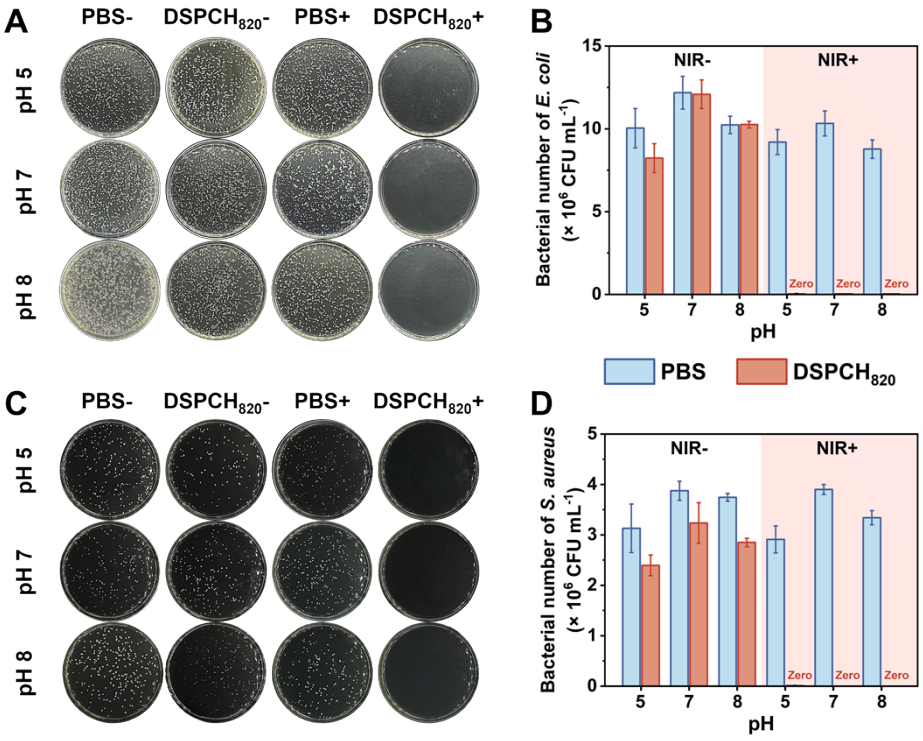

Fig. S17 *In vitro* antibacterial performance of $DSPCH_{820}$ under different pH conditions (pH 5, 7, and 8) with (+) or without (−) NIR irradiation for 10 min. (A, C) Representative photographs of bacterial colonies of *E. coli* (A) and *S. aureus* (C) in different groups. (B, D) Corresponding counting of bacterial number of (B) *E. coli* and (D) *S. aureus* in different groups.

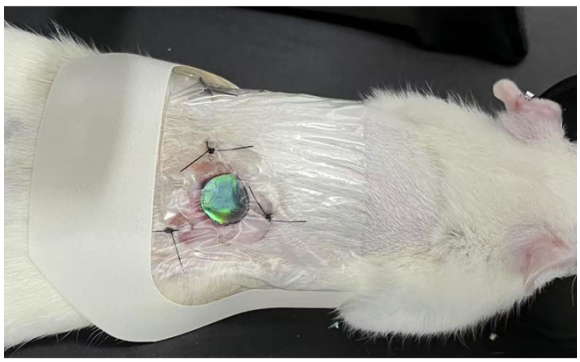

Fig. S18 Representative photograph of the infected SD rat with DSPCH fixed by the 3M polyurethane dressing.

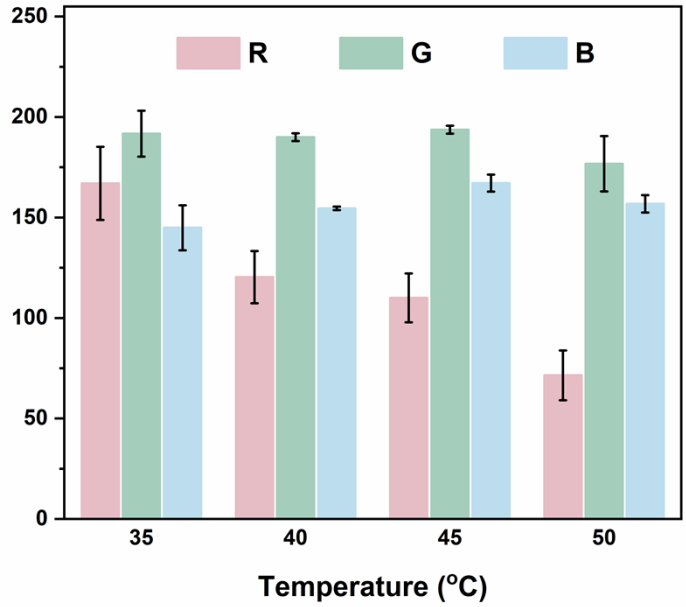

Fig. S19 *R*, *G*, *B* values extracted from optical images (in Fig. 5B) of $DSPCH_{820}$ at different temperatures during the photothermal therapy.

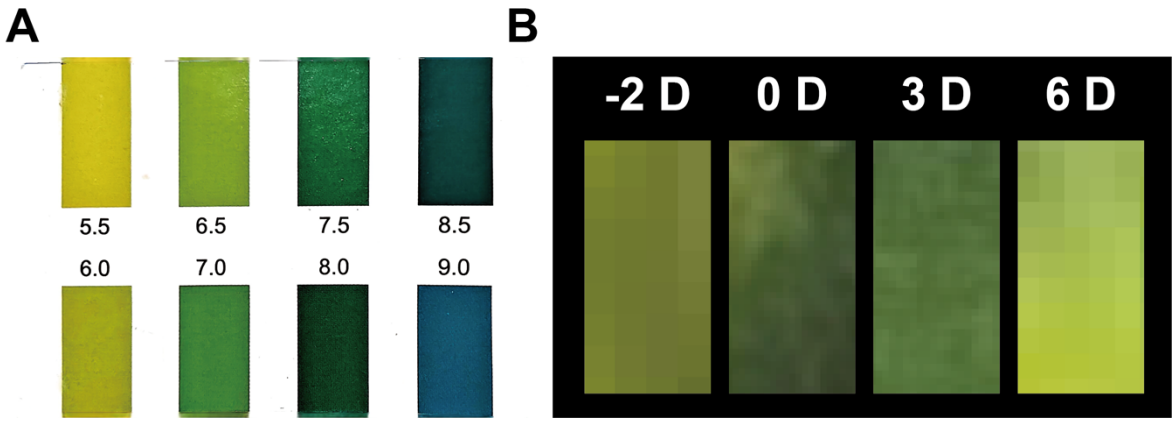

Fig. S20 (A) Standard color card of pH test paper. (B) Optical images of pH test papers for the monitoring of wound pH on days −2, 0, 3, 6.

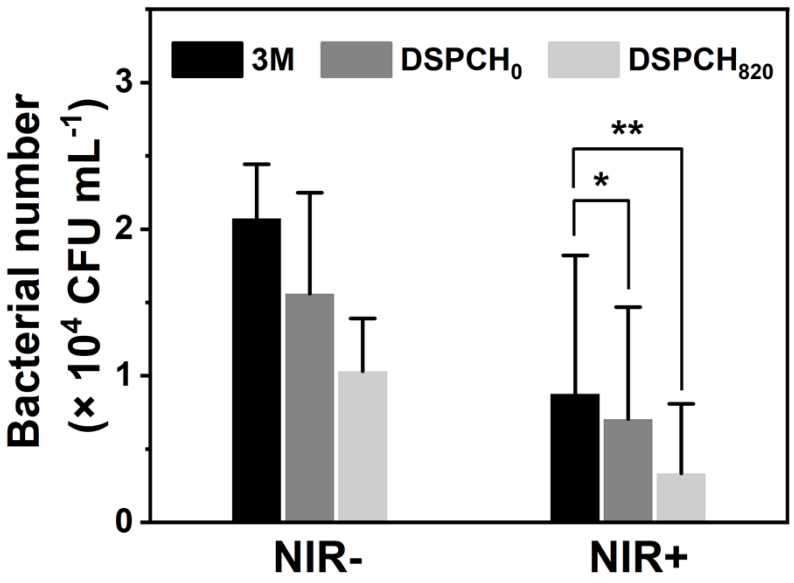

Fig. S21 Number of bacteria from wound exudates in different groups on day 3.

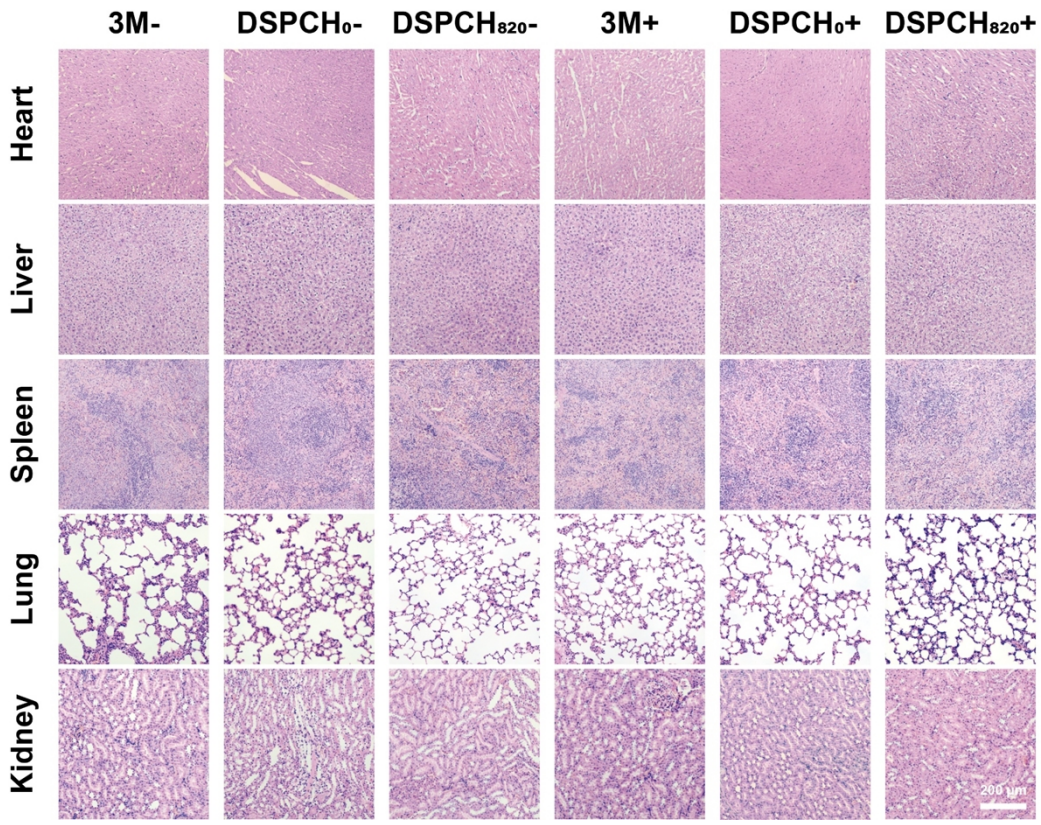

Fig. S22 Hematoxylin and Eosin staining of various organs harvested from SD rats after different treatments on day 10.

Table S1. Photothermal conversion efficiency (PCE) enhancement ratio of this work (PCH_{820}) in comparison to other representative researches.

	Enhanced PCE (%)	Comparison object	Baseline PCE (%)	PCE enhancement ratio[a)]	Reference
This work (PCH_{820} with CB/CNT/MXene)	**32.29/12.7/41.05**	**PCH_0 without CB/CNT/MXene**	**18.48/7.05/21.13**	**1.75/1.80/1.94**	
Bi:Cu_2O@HA+NaHS	16.96	Cu_2O+NaHS	15.7	1.08	Ref. 26[8]
PDA-PEI@N,S-CQDs	28.40	PDA	24.20	1.17	Ref. 27[9]
NanoPcDA2	26.50	NanoPcDA1	19.60	1.35	Ref. 28[10]
Aza-BODIPY NPs	35.00	Free Aza-BODIPY	25.00	1.40	Ref. 29[11]
AuNR (25×7 nm)	--	AuNR (38×10 nm)	--	1.40	Ref. 30[12]
PBA@Ru NCs	42.64	PBA NCs	29.19	1.46	Ref. 31[13]
iAPG	40.96	GO	27.48	1.49	Ref. 32[14]
CSMN2	28.80	CSMN0	19.30	1.49	Ref. 33[15]
Bi-Ag NPs	30.00	Bi NPs	20.00	1.50	Ref. 34[16]
BNFs	20.65	SBNPs	13.69	1.51	Ref. 35[17]
AuPt@CuS NSs	41.56	CuS NSs	26.83	1.55	Ref. 36[18]
P($_L$-DOPA)-C_6DQ-0.014	25.50	PDA	16.50	1.55	Ref. 37[19]
PDA@Ag@GOx	30.20	PDA	18.3	1.65	Ref. 38[20]

[a)] PCE enhancement ratio is calculated as the ratio of enhanced PCE to baseline PCE.

Table S2. Structural color saturation and chromatism (ΔE) of DSPCH at different pH, which are calculated according to the literature.[6]

pH	$R^{a)}$	$G^{a)}$	$B^{a)}$	Saturation[b)] (%)	$L^{*c)}$	$a^{*c)}$	$b^{*c)}$	$\Delta E^{d)}$
4	113.448	54.562	48.698	0.57075	30.45	24.48	37.68	0
5	191.006	136.963	104.148	0.1718	61.96	18.35	26.21	34.08838
6	150.633	142.434	94.891	0.37005	59.03	−2.3	26.5	40.73054
7	58.019	124.075	65.114	0.53239	46.62	−32.09	25.4	60.10351
8	60.349	115.926	78.868	0.47942	44.22	−26.05	14.63	57.22059
9	45.81	156.99	105.207	0.7082	57.68	−41.75	17.81	74.31489

[a)] R, G, B values are extracted from optical images using ImageJ software.

[b)] Structural color saturation values are calculated through equation $Saturation\ (\%) = (\max(R, G, B) - \min(R, G, B))/\max(R, G, B)$.

[c)] L^*, a^*, b^* values are transferred from R, G, B values, where L^*, a^*, and b^* denote lightness, red/green value, and yellow/blue value, respectively.

[d)] ΔE values are calculated relative to the state at pH 4 through the equation $\Delta E = \sqrt{(\Delta L*)^2 + (\Delta a*)^2 + (\Delta b*)^2}$.

Table S3. Comparison of visual detection sensitivity for pH between this work and other representative researches *via* *R*, *G*, *B* values extraction and analysis of material colors at varied pH levels.

Reference	Testing range of pH	*RGB*-pH dependence	$\left\|\frac{\Delta(R/G)}{\Delta pH}\right\|$ a)	$\left\|\frac{\Delta(R/B)}{\Delta pH}\right\|$ a)
This work	4–9	$R/G = 10.14 * e^{(-pH/2.52)} + 0.01$ $R/B = 6.91 * e^{(-pH/8.53)} - 1.98$	0.36	0.38
[21]	4–7	$R/G = -0.305 * pH + 2.91$	0.31	--
[22]	4–6	--	0.20	0.22
[23]	5–9	$R/G = 11.4 * e^{(-pH/1.9)} + 0.75$ $R/B = 4.9 * e^{(-pH/2.3)} + 0.61$	0.18	0.12
[24]	2–12	--	0.0070	0.013
[25]	5–9	$R/B = 0.01169 * pH + 0.87623$	--	0.013
[26]	2–11	--	0.099	0.0022

a) Here, the sensitivity of visual pH detection is quantified by $\left|\frac{\Delta(R/G)}{\Delta pH}\right|$ or $\left|\frac{\Delta(R/B)}{\Delta pH}\right|$, representing the magnitude of colorimetric change per unit pH variation within the corresponding detection range. *R*/*G* or *R*/*B* values are derived either by substituting pH values into a pre-established fitting equation or by calculating chromatic differences based on provided *RGB* values.

Table S4. Structural color saturation and chromatism (ΔE) of DSPCH at various temperatures. ΔE is calculated relative to the state at 35 °C.

Temperature (°C)	*R*	*G*	*B*	Saturation (%)	*L**	*a**	*b**	ΔE
35	116.577	109.077	70.827	39.244	46.02	−1.51	22.5	0
40	170.979	170.206	104.866	38.667	68.61	−7.05	33.75	25.83723
45	213.262	208.083	141.833	33.494	82.77	−5.47	33.64	38.60497
50	225.473	250.351	149.676	40.214	94.92	−19.78	45.32	56.97153
55	131.322	183.359	126.978	30.749	69.79	−26.17	23.04	34.25522
60	92.835	115.738	115.022	19.789	46.88	−8.84	−2.54	26.10498

Table S5. Comparison of detection time between this work and other representative researches for temperature monitoring.

Reference	Material	Monitoring signal	Detection time (min)
This work	PDMAEMA-based PCH	Colorimetric signal	< 1
[27]	PS@GO-PNIPAm PCH	Colorimetric signal	2
[28]	AgNPs-DMAB-FPF	Raman signal	2
[29]	PNIPAm-co-VFc MG interferometer	Colorimetric signal	5
[30]	PDMAPS/P(DEAM-co-DMAM)/PCA-Na)	Electrical signal	15
[31]	P(NIPAAM-co-AAc)	Colorimetric signal	20
[32]	N-GCDs/BSA-AuNCs/PVA-SA	Fluorescence signal	30

Table S6. *R*, *G*, *B* values of $DSPCH_{820}$ extracted from optical images taken on days -2, 0, 3, 6. *R*/*B* and *R*/*G* values are calculated to estimate pH according to fitted standard curves in Figure S10.

Day	*R*	*G*	*B*	*R*/*B*	*R*/*G*
	86.612	124.4	65.675	1.3188	0.69624
−2	88.112	129.125	88.112	1	0.68238
	101.238	140.675	79.5	1.27343	0.71966
	50.975	104.15	99.925	0.51013	0.48944
0	37.112	84.012	98.138	0.37816	0.44175
	35.188	80.35	92.688	0.37964	0.43793
	84.725	134.575	54.475	1.5553	0.62957
3	82.9	124.65	52.3	1.58509	0.66506
	80.025	121.062	53.325	1.5007	0.66102
	184.6	171.75	147.738	1.24951	1.07482
6	191.025	148.062	123.875	1.54208	1.29017
	212.338	210.138	116.662	1.82011	1.01047

References

[1] Yavuz, G.; Felgueiras, H. P.; Ribeiro, A. I.; Seventekin, N.; Zille, A.; Souto, A. P. Dyed Poly(styrene-methyl methacrylate-acrylic acid) Photonic Nanocrystals for Enhanced Structural Color. *ACS Appl. Mater. Interfaces* **2018**, *10* (27), 23285–23294.

[2] Liu, G. J.; Zhou, L.; Fan, Q. G.; Chai, L. Q.; Shao, J. Z. The Vertical Deposition Self-assembly Process and the Formation Mechanism of Poly(styrene-co-methacrylic acid) Photonic Crystals on Polyester Fabrics. *J. Mater. Sci.* **2016**, *51*, 2859–2868.

[3] Nedunchezian, S.; Wu, C. -W.; Wu, S. -C.; Chen, C. -H.; Chang, J. -K.; Wang, C. -K. Characteristic and Chondrogenic Differentiation Analysis of Hybrid Hydrogels Comprised of Hyaluronic Acid Methacryloyl (HAMA), Gelatin Methacryloyl (GelMA), and the Acrylate-Functionalized Nano-Silica Crosslinker. *Polymers* **2022**, *14* (10), 2003.

[4] Cao, Y. Y.; Dou, J. -H.; Zhao, N. -J.; Zhang, S. M.; Zheng, Y. -Q.; Zhang, J. -P.; Wang, J. -Y.; Pei, J.; Wang, Y. P. Highly Efficient NIR-II Photothermal Conversion Based on an Organic Conjugated Polymer. *Chem. Mater.* **2017**, *29* (2), 718–725.

[5] Xie, X. Y.; Zhang, Z. L.; Jiang, Q.; Zheng, S. T.; Yun, Y.; Wu, H.; Li, C. B.; Tian, F.; Su, M.; Li, F. A Rainbow Structural Color by Stretchable Photonic Crystal for Saccharide Identification. *ACS Nano* **2022**, *16* (12), 20094–20099.

[6] Yang, X.; Zhang, Z. Y.; Sun, H. Y; Yun, Y.; Xie, H. F.; Tan, Z. Y.; Wang, H. D.; Yang, Y. Q.; Chen, B. D.; Teng, H. R.; Yang, M. T.; Sun, M. T.; Song, Y. L.; Su, M. Multidimensional Resonance Controlled by Critical Size in Printed Binary Colloidal Crystals for High-Contrast Imaging. *J. Am. Chem. Soc.* **2025**, *147*, 3383–3391.

[7] Zhang, Y. H.; Hu, Y. B.; Montelongo, Y.; Hsu, M.; Blyth, J.; Jiang, N.; Yetisen;

A. K. A Conformable Holographic Sensing Bandage for Wound Monitoring. *Adv. Funct. Mater.* **2024**, *34* (16), 2308490.

[8] Cheng, Y. Y.; Bo, H. J.; Qin, R. M.; Chen, F. L.; Xue, F. F.; An, L.; Huang, G.; Tian, Q. Hyaluronic Acid-Coated Bi:Cu_2O: an H_2S-Responsive Agent for Colon Cancer with Targeted Delivery and Enhanced Photothermal Performance. *J. Nanobiotechnol.* **2022**, *20*, 346.

[9] Shu, Q. F.; Liu, J.; Chang, Q.; Liu, C. H.; Wang, H. F.; Xie, Y. J.; Deng, X. Y. Enhanced Photothermal Performance by Carbon Dot-Chelated Polydopamine Nanoparticles. *ACS Biomater. Sci. Eng.* **2021**, *7* (12), 5497–5505.

[10] Zhao, Y. -Y.; Chen, Z. X.; Zhang, L.; Qin, X. -W.; Liu, H.; Zheng, B. -Y.; Ke, M. R.; Huang, J. -D.; Li, X. S. A Self-Degradable Nanostructured Phthalocyanine Assembly with High Photothermal Efficacy to Enhanced Biosecurity in Photothermal Therapy. *Chem. Eng. J.* **2023**, *474*, 145921.

[11] Xu, Y. J.; Feng, T.; Yang, T. S.; Wei, H. J.; Yang, H. R.; Li, G.; Zhao, M. L.; Liu, S. J.; Huang, W.; Zhao, Q. Utilizing Intramolecular Photoinduced Electron Transfer to Enhance Photothermal Tumor Treatment of Aza-BODIPY-Based Near-Infrared Nanoparticles. *ACS Appl. Mater. Interfaces* **2018**, *10* (19), 16299–16307.

[12] Mackey, M. A.; Ali, M. R. K.; Austin, L. A.; Near, R. D.; El-Sayed, M. A. The Most Effective Gold Nanorod Size for Plasmonic Photothermal Therapy: Theory and in vitro Experiments. *J. Phys. Chem.* B **2014**, *118* (5), 1319–1326.

[13] Ma, K. M.; Cao, Y. Y.; Xuan, C. Y.; Yang, J. Y.; Li, F.; Zhe, T. T.; Luo, Q.; Wang, L. Ru Nanoclusters Engineer Prussian Blue Analog Nanocubes for Multiple Active Sites Synergistic Catalysis Enabling High-Performance Bacterial Detection. *Chem. Eng. J.* **2025**, *507*, 160553.

[14] Wang, Z.; Cheng, H.; Sheng, Y.; Chen, Z. K.; Zhu, X. H.; Ren, J. Y.; Zhang, X. G.; Lv, L. Y.; Zhang, H. Q.; Zhou, J. P.; Ding, Y. Biofunctionalized Graphene

Oxide Nanosheet for Amplifying Antitumor Therapy: Multimodal High Drug Encapsulation, Prolonged Hyperthermal Window, and Deep-Site Burst Drug Release. *Biomaterials* **2022**, *287*, 121629.

[15] Shao, W.; Wei, Q. L.; Wang, S. F.; Li, F. Y.; Wu, J. H.; Ren, J. F.; Cao, F. Y.; Liao, H. W.; Gao, J. Q.; Zhou, M.; Ling, D. S. Molecular Engineering of D-A-D Conjugated Small Molecule Nanoparticles for High Performance NIR-II Photothermal Therapy. *Mater. Horiz.* **2020**, *7* (5), 1379–1386.

[16] Ma, S. H.; Luo, X.; Kong, J. L.; Li, X. Y.; Cao, Z. Q.; Wang, X.; Cai, W. Y.; Wang, L.; Ran, G. Plasmonic Silver Loaded Hybrid Bi-Ag Nanoalloys for Highly Efficient Disinfection by Enhancing Photothermal Performance and Interface Capability. *Chem. Eng. J.* **2022**, *450*, 138016.

[17] Wen, J.; Liu, C.; Liu, J.; Wang, L.; Miao, S.; Chen, D. Q.; Wang, Q. Y.; Huo, M. R.; Shen, Y. Dextran 40 Hybrid Biomimetic Bismuth-Nanoflower Designed for NIR II-Triggered Hypoxic Tumor Thermoradiotherapy via Macrophage Escape. *Carbohydr. Polym.* **2023**, *310*, 120697.

[18] Cai, R.; Xiang, H. D.; Yang, D.; Lin, K. -T.; Wu, Y. Z.; Zhou, R. Y.; Gu, Z. J.; Yan, L.; Zhao, Y. L.; Tan, W. H. Plasmonic AuPt@CuS Heterostructure with Enhanced Synergistic Efficacy for Radiophotothermal Therapy. *J. Am. Chem. Soc.* **2021**, *143* (39), 16113–16127.

[19] Wang, X. H.; Zhang, J. H.; Li, H. T.; Zhang, R.; Yang, X. X.; Li, W. J.; Li, Z.; Gu, Z. P.; Li, Y. W. Quaternary Ammonium Assisted Synthesis of Melanin-Like Poly($_{L}$-DOPA) Nanoparticles with a Boosted Photothermal Effect. *ACS Appl. Mater. Interfaces* **2024**, *16* (17), 22493–22503.

[20] Yu, S.; Shen, H.; Chen, X.; Wang, H.; He, C. Y.; Hu, T. H.; Cao, G.; Zhang, L. A cascade nanosystem with “Triple-Linkage” Eeffect for Enhanced Photothermal and Activatable Metal Ion Therapy for Hepatocellular Carcinoma. *J. Nanobiotechnol.* **2024**, *22*, 334.

[21] Wen, Y.; Wang, L. -P.; Yu, Y. -L.; Chen, S. A 3D-Printed Dual-Mode Gel

Microspheres Kit for Multipath Smart Detection of Multiple Targets in Urine. *Talanta* **2025**, *292*, 127889.

[22] Park, H.; Koh, Y. G.; Lee, W. Smartphone-Based Colorimetric Analysis of Structural Colors From pH-Responsive Photonic Gel. *Sens. Actuators, B.* **2021**, *345*, 130359.

[23] Xu, Z.; Fan, J. L.; Tian, W. G.; Ji, X.; Cui, Y. Q.; Nan, Q. Y.; Sun, F. F.; Zhang, J. Cellulose-Based pH-Responsive Janus Dressing with Unidirectional Moisture Drainage for Exudate Management and Diabetic Wounds Healing. *Adv. Funct. Mater.* **2023**, *34* (3), 2307449.

[24] Forjan, E.; Marković, M. -P.; Kassal, P.; Vrsaljko, D. Development and Characterization of Litmus-Based pH Sensor Films for Real-Time Monitoring in 3D Printed Microreactor Channels. *J. Sol-Gel Sci. Technol.* **2025**, *115*, 1–16.

[25] Huo, K. -F.; Zhang, J. F.; Lin, T.; Zhang, Y. Y.; Liu, Y.; Liu, X. Y. Colorimetric and Fluorescent Dual-Mode pH Sensor with PMIA as Substrate and CQDs as Probe for High Accuracy Detection of Full Range pH. *Dyes and Pigm.* **2023**, *219*, 111574.

[26] Marković, M. -P.; Kassal, P.; Vrsaljko, D. Design and Fabrication of a pH Sensor-Coated Microreactor System. *IEEE Sens. J.* **2024**, *24* (20), 32090–32097.

[27] Shen, H. F.; Lin, Q.; Tang, H. C.; Tian, Y. Q.; Zhang, X. Y. Fabrication of Temperature- and Alcohol-Responsive Photonic Crystal Hydrogel and Its Application for Sustained Drug Release. *Langmuir* **2022**, *38* (12), 3785–3794.

[28] Liu, L. L.; Li, D.; Deng, W. Stimuli-Responsive Microgels with Fluorescent and SERS Activities for Water and Temperature Sensing. *Biosens. and Bioelectron.* **2021**, *180*, 113138.

[29] Wang, Y. J.; Li, C.; Shen, M. J.; Ding, W. J.; Xu, X. Y.; Han, L.; Zhu, W. F.; Guo, Z. Z.; Wang, L. Y.; Hu, L. Beetle-Inspired Responsive Photonic Microgel Assemblies for Multi-sensing Enhanced by Machine Learning. *Biosens. and Bioelectron.* **2025**, *286*, 117581.

[30] Zhou, B.; Yuan, W. Z. Bidirectional Temperature-Responsive Thermochromism and Stretchable Hydrogel Sensor for Human Motion/Health Detection, Visual Signal Transmission, and Smart Windows. *Chem. Eng. J.* **2025**, *521*, 166939.

[31] Xue, H.; Liu, F.; Wang, Z.; Liu, D. L.; Zhou, L.; Su, W. B.; Niu, S. C.; Han, Z. W.; Ren, L. Q. Bio-Inspired Dual-Responsive Photonic Crystal with Smart Responsive Hydrogel for pH and Temperature Detection. *Mater. Des.* **2023**, *233*, 112242.

[32] Cao, Y. R.; Chen, M. T.; Li, J. L.; Liu, W. P.; Zhu, H. S.; Liu, Y. J. Continuous Monitoring of Temperature and Freshness in Cold Chain Transport Based on the Dual-Responsive Fluorescent Hydrogel. *Food Chem.* **2024**, *438*, 137981.